# SUPPLEMENTARY INFORMATION

## Inferring interiors and structural history of top-shaped asteroids from external properties of asteroid (101955) Bennu

**Authors:** Yun Zhang[1,2], Patrick Michel[1], Olivier S. Barnouin[3], James H. Roberts[3], Michael G. Daly[4], Ronald-L. Ballouz[3,5], Kevin J. Walsh[6], Derek C. Richardson[7], Christine M. Hartzell[2], Dante S. Lauretta[5]

[1]*Université Côte d'Azur, Observatoire de la Côte d'Azur, CNRS, Laboratoire Lagrange, Nice, France.*

[2]*Department of Aerospace Engineering, University of Maryland, College Park, MD, USA.*

[3]*The Johns Hopkins University, Applied Physics Laboratory, Laurel, MD, USA.*

[4]*The Centre for Research in Earth and Space Science, York University, Toronto, ON, Canada.*

[5]*Lunar and Planetary Laboratory, University of Arizona, Tucson, AZ, USA.*

[6]*Southwest Research Institute, Boulder, CO, USA.*

[7]*Department of Astronomy, University of Maryland, College Park, MD, USA.*

**To whom correspondence should be addressed; Email: yun.zhang@oca.eu*

# Contents

## Supplementary Table



## Supplementary Figures

Supplementary Table 1: Material properties ($\phi$ and $C$), critical spin period ($T_{\text{crit}}$), and failure mode under spinup loading of the Bennu-like rubble-pile model with different interparticle parameter sets ($\mu_S$, $\beta$, and $c$).

| $\mu_S$ | $\beta$ | $c$ (Pa) | Core density[a] | Structure[b] | $\phi$ (°) | $C$ (Pa) | $T_{\text{crit}}$ (h)[c] | Failure mode[d] |
|---|---|---|---|---|---|---|---|---|
| 0.2 | 0.3 | 0 | Underdense | Homogeneous | 29 | 0 | 3.77 | Types I & II[e] |
| 0.2 | 0.3 | 0 | Uniform | Homogeneous | 29 | 0 | 3.76 | Types I & II |
| 0.2 | 0.3 | 0 | Denser | Homogeneous | 29 | 0 | 3.75 | Types I & II[f] |
| 0.2 | 0.3 | 3 | Underdense | Homogeneous | 29 | 0.038 | 3.77 | Types I & II |
| 0.2 | 0.3 | 10 | Underdense | Homogeneous | 29 | 0.13 | 3.74 | Types I & II |
| 0.2 | 0.3 | 30 | Underdense | Homogeneous | 29 | 0.38 | 3.68 | Types I & II |
| 0.2 | 0.3 | 50 | Underdense | Homogeneous | 29 | 0.65 | 3.62 | Types I & II |
| 0.2 | 0.3 | 60 | Underdense | Homogeneous | 29 | 0.78 | 3.58 | Type II[g] |
| 0.2 | 0.3 | 100 | Underdense | Homogeneous | 29 | 1.3 | 3.47 | Type II |
| 0.2 | 0.3 | 400 | Underdense | Homogeneous | 29 | 5.2 | 2.93 | Type IV |
| 0.2 | 0.3 | 800 | Underdense | Homogeneous | 29 | 10 | 2.51 | Type IV[k] |
| 0.2 | 0.3 | 1000 | Underdense | Homogeneous | 29 | 13 | 2.34 | Type IV |
| 0.4 | 0.4 | 0 | Underdense | Homogeneous | 32 | 0 | 3.53 | Types I, II & III[h] |
| 0.4 | 0.4 | 0 | Uniform | Homogeneous | 32 | 0 | 3.52 | Types I, II & III |
| 0.4 | 0.4 | 0 | Denser | Homogeneous | 32 | 0 | 3.52 | Types I, II & III |
| 0.6 | 0.5 | 0 | Underdense | Homogeneous | 35 | 0 | 3.46 | Types I & III[i] |
| 0.6 | 0.5 | 0 | Uniform | Homogeneous | 35 | 0 | 3.46 | Types I & III |
| 0.6 | 0.5 | 0 | Denser | Homogeneous | 35 | 0 | 3.46 | Types I & III |
| 0.6 | 0.5 | 3 | Underdense | Homogeneous | 35 | 0.11 | 3.44 | Types I & III |
| 0.6 | 0.5 | 10 | Underdense | Homogeneous | 35 | 0.35 | 3.41 | Types I & III |
| 0.6 | 0.5 | 50 | Underdense | Homogeneous | 35 | 1.7 | 3.31 | Types I & III |
| 0.6 | 0.5 | 100 | Underdense | Homogeneous | 35 | 3.5 | 3.02 | Types II & III |
| 0.6 | 0.5 | 300 | Underdense | Homogeneous | 35 | 11 | 2.50 | Type IV |
| 1.0 | 0.8 | 0 | Underdense | Homogeneous | 40 | 0 | 3.42 | Types I & III[j] |
| 1.0 | 0.8 | 0 | Uniform | Homogeneous | 40 | 0 | 3.43 | Types I & III |
| 1.0 | 0.8 | 0 | Denser | Homogeneous | 40 | 0 | 3.44 | Types I & III |
| 1.0 | 0.8 | 3 | Underdense | Homogeneous | 40 | 0.30 | 3.40 | Types I & III |
| 1.0 | 0.8 | 10 | Underdense | Homogeneous | 40 | 1.0 | 3.32 | Types I & III |

Continuation of Table 1

| $\mu_S$ | $\beta$ | $c$ (Pa) | Core density[a] | Structure[b] | $\phi$ (°) | $C$ (Pa) | $T_{\text{crit}}$ (h)[c] | Failure mode[d] |
|---|---|---|---|---|---|---|---|---|
| 1.0 | 0.8 | 50 | Underdense | Homogeneous | 40 | 5.4 | 2.88 | Types II & III |
| 1.0 | 0.8 | 100 | Underdense | Homogeneous | 40 | 11 | 2.57 | Type IV |
| 1.0 | 0.8 | 200 | Underdense | Homogeneous | 40 | 22 | 2.15 | Type IV |
| 0.2 | 0.3 | 60 | Underdense | Layered | 29 | 0.78 | 3.58 | Types I & II |
| 0.2 | 0.3 | 80 | Underdense | Layered | 29 | 1.0 | 3.54 | Types I & II[l] |
| 0.2 | 0.3 | 100 | Underdense | Layered | 29 | 1.3 | 3.49 | Types I, II & III[m] |
| 0.2 | 0.3 | 200 | Underdense | Layered | 29 | 2.6 | 3.48 | Types I & III[n] |
| 0.2 | 0.3 | 400 | Underdense | Layered | 29 | 5.2 | 3.48 | Types I & III |
| 0.2 | 0.3 | 800 | Underdense | Layered | 29 | 10 | 3.48 | Types I & III |
| 0.2 | 0.3 | 800 | Underdense | Heterogeneous | 29 | 10 | 3.57 | Types I & II |
| 0.2 | 0.3 | 8000 | Underdense | Heterogeneous | 29 | 100 | 3.56 | Types I & II[o] |
| 0.4 | 0.4 | 4300 | Underdense | Heterogeneous | 32 | 100 | 3.35 | Types I, II & III |
| 0.6 | 0.5 | 2800 | Underdense | Heterogeneous | 35 | 100 | 3.28 | Types I & III[p] |
| 1.0 | 0.8 | 900 | Underdense | Heterogeneous | 40 | 100 | 3.24 | Types I & III |

[a] The centre 100-meter-radius region of the rubble-pile model is assigned a density lower than ("Underdense"; $\rho_{\text{inter}} = 0.8\rho_{\text{outer}}$), equal to ("Uniform"; $\rho_{\text{inter}} = \rho_{\text{outer}}$), or higher than ("Denser"; $\rho_{\text{inter}} = 1.2\rho_{\text{outer}}$) the density of the outer region.

[b] All rubble piles use the same $\mu_S$ and $\beta$ to solve the contact interactions for all constituent particles (Methods Section Soft-sphere discrete element method). A homogeneous structure also uses the same $c$ overall for the body, while a layered structure has a 25-meter-depth surface layer with $c = 0$ Pa and a cohesive interior with $c$ given in the third column. A heterogeneous structure has five cohesive regions with the given $c$ in the third column and a coheionless matrix (see Fig. 5a).

[c] The critical spin period is measured at the point when the body's longest axis length has changed by 1.5%. As this pronounced change in the appearance lags behind the structural failure, this value is slightly shorter than the actual critical spin period (ref. [51]).

Continuation of Table 1

| $\mu_S$ | $\beta$ | $c$ (Pa) | Core density[a] | Structure[b] | $\phi$ (°) | $C$ (Pa) | $T_{\rm crit}$ (h)[c] | Failure mode[d] |
|---|---|---|---|---|---|---|---|---|

[d] Type I: local surface landslides, where at least one surface particle having displacement >1 m is detected during spinup; Type II: internal deformation, where changes in the shortest-to-longest axis ratio of the rubble-pile interior exceed 3% (i.e., the 1.5% changes in axis lengths at the end of spinup can be attributed to the deformation of the internal structure; excluding the cases having Type IV failure mode); Type III: surface mass shedding, where at least one surface particle is lofted above the surface (excluding the cases having Type IV failure mode); Type IV: tensile disruption, where surface fracture lineaments are detected during structural reconfiguration (see Supplementary Movies 1–12 for examples of these four failure behaviours).

[e] The structural evolution of this case is presented in Supplementary Movie 1.

[f] See Supplementary Movie 2.

[g] See Supplementary Movie 3.

[h] See Supplementary Movie 4.

[i] See Supplementary Movie 5.

[j] See Supplementary Movie 6.

[k] See Supplementary Movie 7.

[l] See Supplementary Movie 8.

[m] See Supplementary Movie 9.

[n] See Supplementary Movie 10.

[o] See Supplementary Movie 11.

[p] See Supplementary Movie 12.

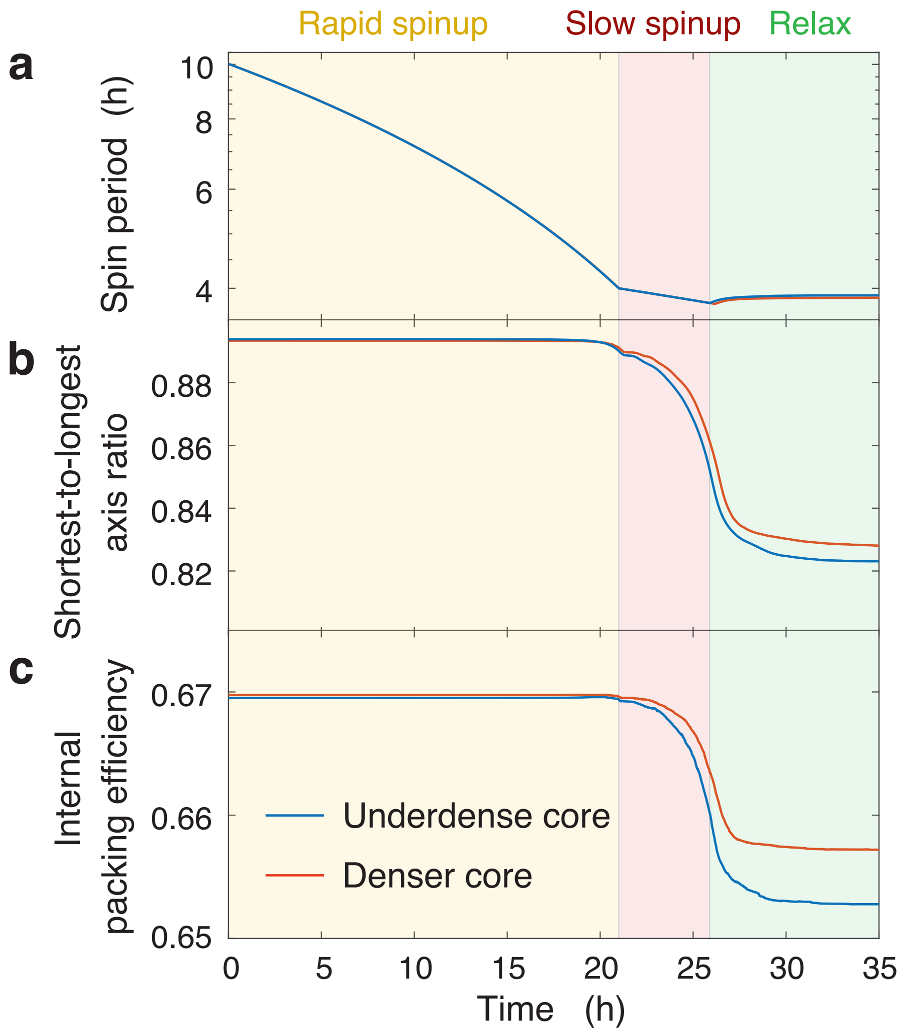


Supplementary Figure 1: **YORP-induced spinup evolution of the Bennu-shaped rubble-pile model with $\phi = 29^{\circ}$ and $C = 0$ Pa.** The rubble pile is forced to rotate following the predefined spin period, including rapid and slow spinup stages (Panel **a**). When the longest axis length has changed by 1.5%, the spinup ceases, and the body evolves under its self-gravity. The spinup process leads to a more oblate shape (Panel **b**) and a lower internal packing efficiency (Panel **c**). Supplementary Movies 1–2 visualise this process. The results for different internal density distributions are denoted in different colours as indicated in the legend. Both cases can generate a more dilute core, supporting the idea that Bennu's underdense core could be formed through such internal deformation processes regardless of the initial density distribution. Source data are provided as a Source Data file.

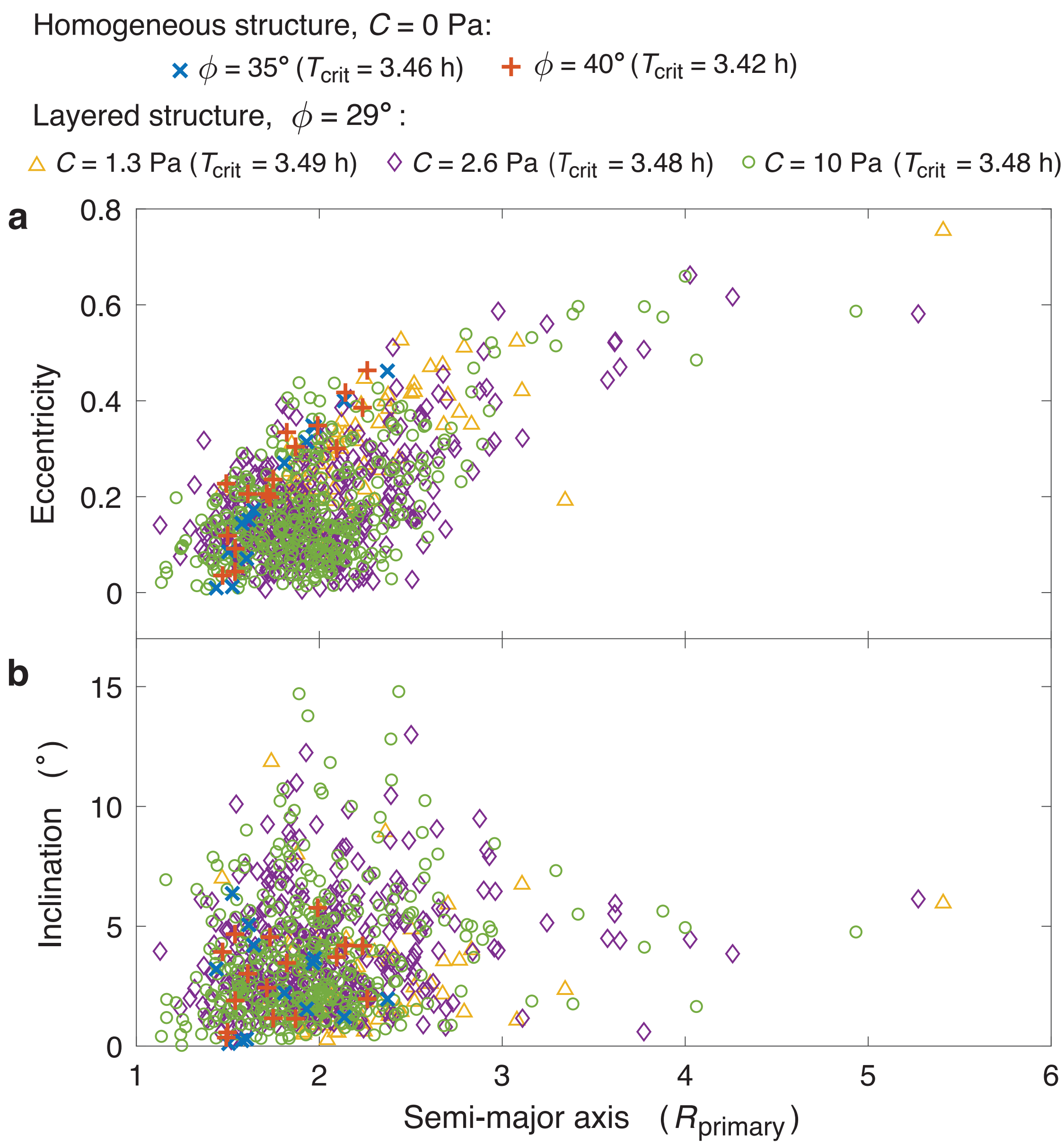


Supplementary Figure 2: **Orbital elements of YORP-induced ejecta around the Bennu-shaped rubble-pile model. a**, orbital eccentricity; **b**, orbital inclination. The semi-major axis is expressed as a ratio relative to the equatorial radius of the primary $R_{\mathrm{primary}}$. The symbols denote the results for tests with different friction angles $\phi$ and cohesive strength $C$, as indicated on the top. The results are recorded at the moment 40 h after the initial structural failure for each case. Source data are provided as a Source Data file.

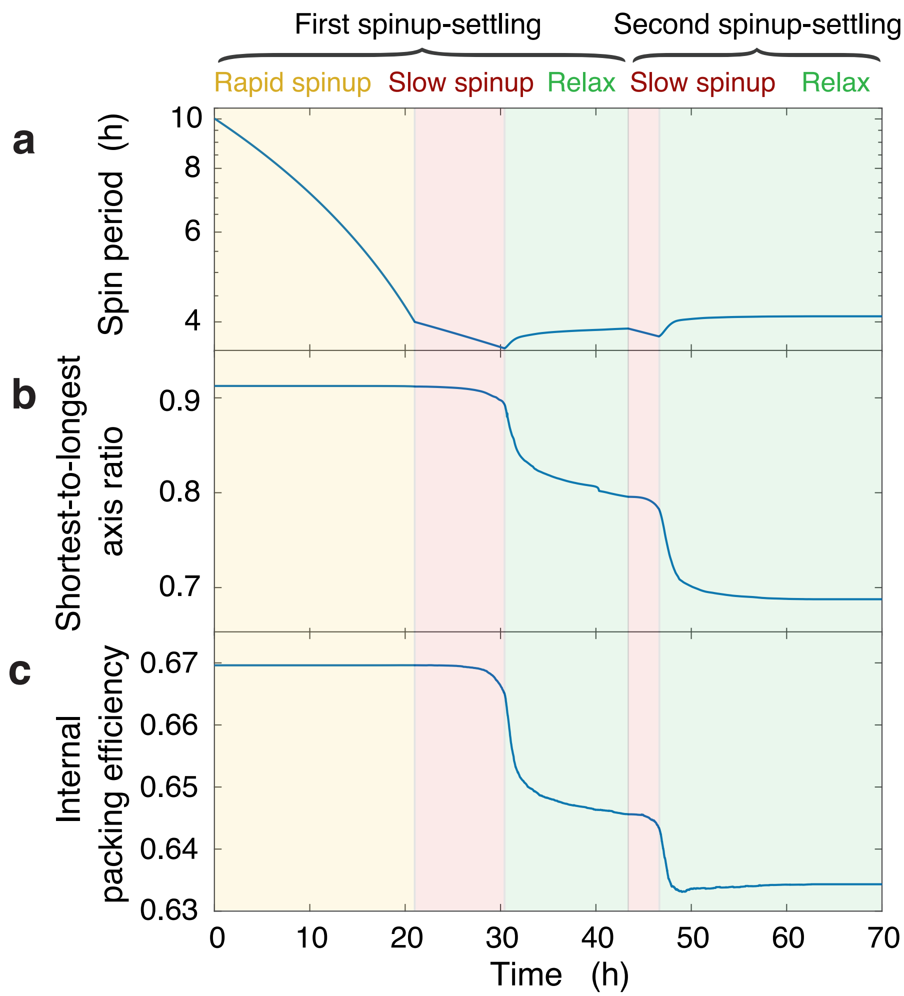


Supplementary Figure 3: **Structural evolution of a heterogeneous rubble pile with $\phi = 29°$ and $C = 0$ Pa undergoing two consecutive spinup-settling paths.** **a**, spin period; **b**, axis ratio; **c**, internal pacing efficiency. During each path, the spinup ceases when the longest axis length has changed by 1.5%, and the body evolves under its self-gravity (see Supplementary Movie 11). The failure behaviours during these two paths are identical, showing that consecutive YORP-spinup cycles could lead a rubble pile to a more oblate shape with a more dilute core. Source data are provided as a Source Data file.

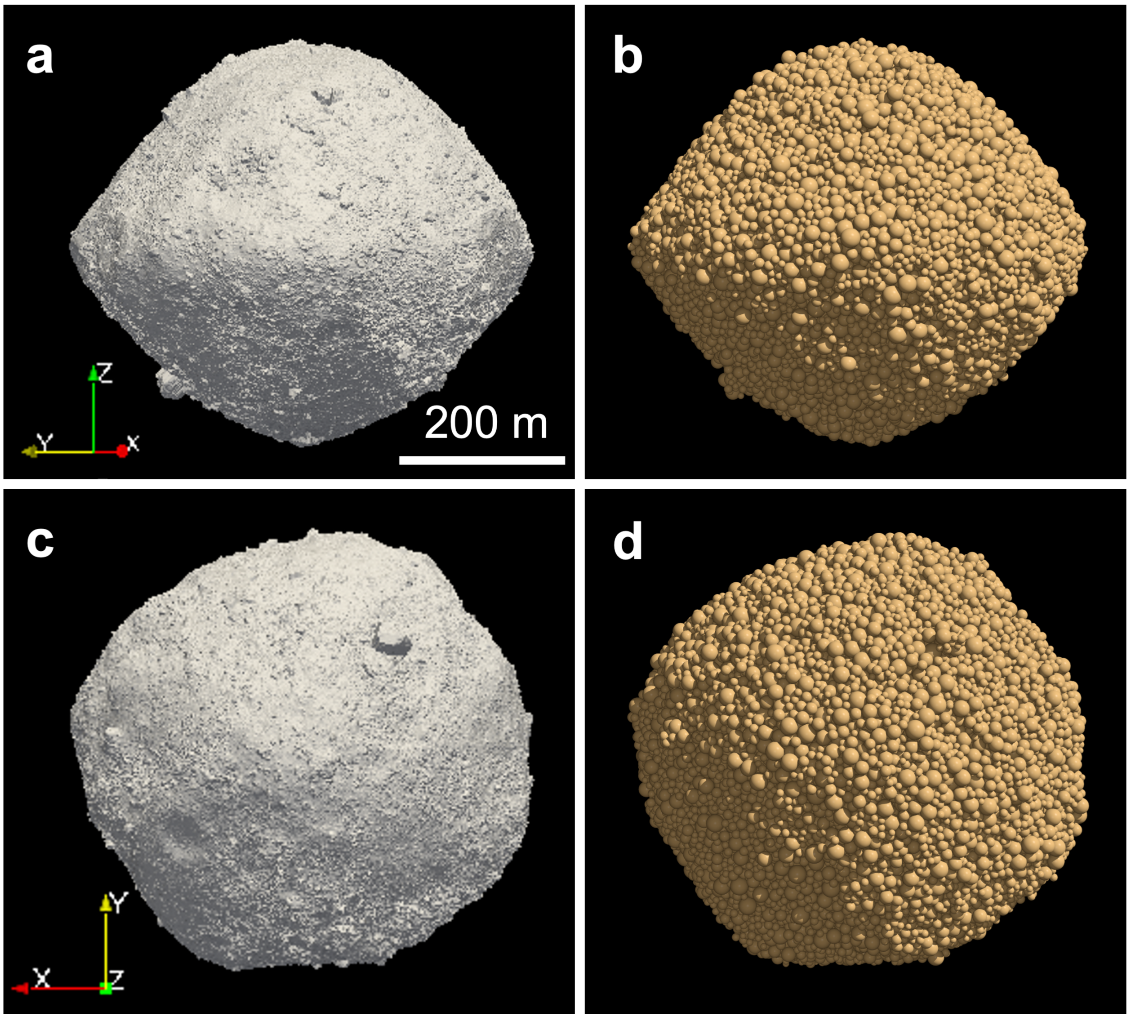


Supplementary Figure 4: **Comparisons of the Bennu OSIRIS-REx Laser Altimeter (OLA) shape model (a, c) and the corresponding rubble-pile model used in this study (b, d).** The top and bottom panels present the top view and side view, respectively. The OLA shape model (v20) is available from the Small Body Mapping Tool (SBMT) at `https://sbmt.jhuapl.edu/Object-Template.php?obj=77`.

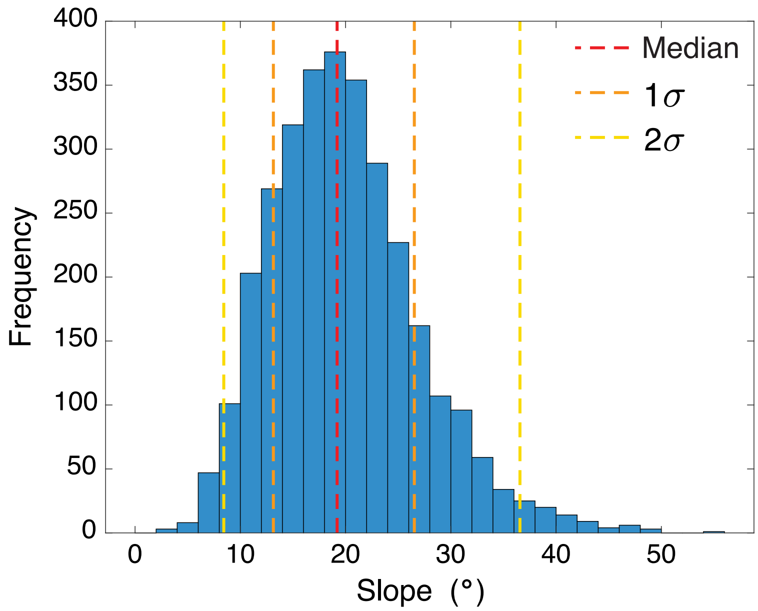


Supplementary Figure 5: **Surface slope distribution of the Bennu-shaped rubble-pile model at Bennu's current spin period of $T = 4.296$ h.** The surface slope is calculated for top-surface particles using Eq. (8) (see Methods). The width of each bin is $2^{\circ}$. Source data are provided as a Source Data file.

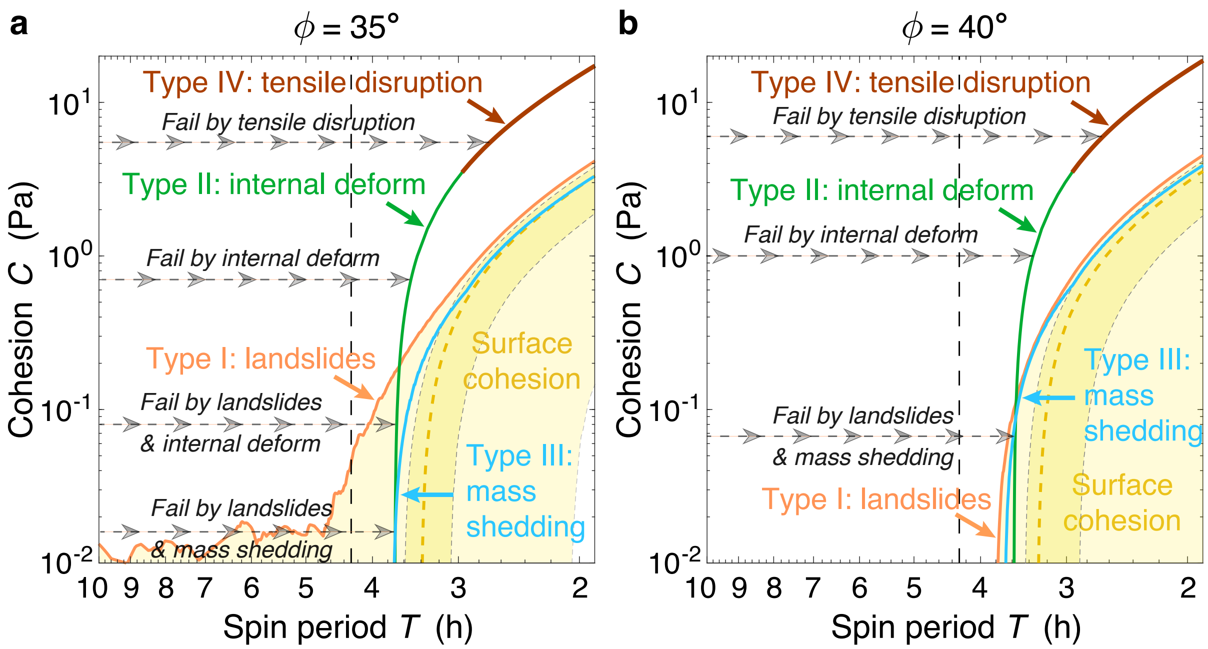


Supplementary Figure 6: **Bennu-shaped cohesive rubble-pile failure mode diagram.** Similar to Fig. 3b, but for $\phi = 35°$ (**a**) and $\phi = 40°$ (**b**). At Bennu's current spin period (as indicated by the black vertical dashed line), surface mass movement is suppressed in the case of $\phi = 35°$ for $C \gtrsim 0.05$ Pa and in the case of $\phi = 40°$ without any cohesion. Source Data are provided as a Source Data file.